# Visual Detectability of the Convair 580

Cyrus Minwalla*,
*MTG Ltd., Ottawa, ON, K2G 7A5, Canada*

Andrew Price†, Sebastian Ghinet‡
*National Research Council Canada, Ottawa, ON, K1V 1J8, Canada*

**Early detection of low-flying aircraft in the vicinity of uncontrolled aerodromes is important for nuisance awareness and public safety. Visual and acoustic modalities can be employed to achieve this goal. This paper focuses on the visual aspect, and as such, describes an empirical technique for estimating the visual detection range of a typical low-flying aircraft under clear sky conditions. The figure of merit, $R_0$, establishes the range at first detection, and can be experimentally evaluated from a captured image sequence of an inbound target. Flight tests were conducted at the Smith Falls - Montague airfield in eastern Ontario, Canada. A fully instrumented Convair 580, a twin-turboprop aircraft equipped with a high resolution data acquisition system, was used for the test. Glide-slope inbound approaches and level-flight cloverleaf patterns were flown over the airfield to simulate typical behaviour of low-flying aircraft. The metric $R_0$ is measured from contrast-to-noise ratio curves extracted over individual events, with each curve resulting in a single $R_0$ estimate. Results indicate an average detection range of approximately 8 km for the Convair under clear sky conditions with $< 20\%$ broken clouds (sufficiently clear sky). Changing environmental conditions over the course of the event caused significant variability in the observed $R_0$ values computed from individual events.**

## I. Introduction

Low-flying aircraft near uncontrolled aerodromes present an annoyance to local residents in the surrounding built-up areas. Many uncontrolled aerodromes in North America are located within small communities and lack adequate buffering (unused land) or shielding (barriers) between the houses and the aerodrome. Early identification of such aircraft could aid in public awareness initiatives, thereby reducing the nuisance aspect.

Early detection of aircraft is crucial for nuisance warning. ADS-B is an excellent candidate for cooperative, long-range monitoring of air traffic. In Canada, however, personal and hobby aircraft are not mandated to carry an ADS-B transponder, limiting the efficacy of this approach. In a non-cooperative environment, aircraft can be detected by a variety of sensors, of which acoustic and visual are the most common. These sensors may operate individually or be jointly fused for a more robust estimate. Approaches to sensor fusion are numerous, and the specific model depends on the relative position, orientation and configuration of the sensors: For instance, an isotropic acoustic system can serve as the early, long-range detector, and cue a pan-tilt-zoom camera for localization and identification. Conversely, a high-spatial-resolution, wide field-of-view camera array [1] may perform initial long-range detection and subsequently cue a directional audio system for signature analysis. The focus of this work is early warning through visual detection, in particular, the use of electro-optical machine-vision cameras as the sense modality. These cameras are prominent in mobile robotics and unmanned aircraft systems (UAS), and, given their practicality and commercial availability, are ideally suited for the present application. A methodology for estimating the maximum detection range from image sequences was adapted from prior efforts on unmanned aircraft collision-course estimation and counter-UAS applications, and employed to assess the detection range of an instrumented Convair 580 aircraft supplied by the National Research Council of Canada.

The remainder of this paper is structured as follows: Section II describes the technique underpinning this work, followed by a description of the experimental setup in Section III, with results and analysis presented in Section IV, followed by a conclusion in Section V.

## II. Methodology

The computed maximum detection range of the camera system, $R_0$, is the metric of interest in this work. Such quantified estimates are more reliable than human observations from attentive vision under ideal circumstances and

*Principal, cyrus@minwalla.org
†Research Officer, Aeroacoustics and Structural Dynamics Group - Flight Research Lab - AEROSPACE
‡Research Officer, Aeroacoustics and Structural Dynamics Group - Flight Research Lab - AEROSPACE

significantly more robust under cognitive load [2]. A quantified technique for the assessment of visual detection range is derived based on this $R_0$ figure of merit. Here, $R_0$ is defined as the maximum detection range at which an attentive human observer is expected to detect the aircraft under clear sky, high-visibility conditions.

Applicability of the technique in determining human visual detection range under similar circumstances is subject to the following comparable attributes: Image sensors attuned to the visible spectrum exhibit a spectral responsivity curve that closely aligns with the spectral response of the human eye. In addition, machine vision cameras outfitted with typical lenses maintain a constant spatial resolution across the field of view, unlike the human eye, where spatial resolution degrades rapidly beyond the macular region. Furthermore, automated algorithms written for machine vision cameras treat all pixels equally (unless explicitly weighted) and are not subject to attentive vision artifacts such as saccades, attention deficit, external distractions or changes in cognitive load. Machine vision cameras do, however, possess a limited dynamic range compared to the human eye, and as such are susceptible to saturation and noise-floor effects.

Despite the trade-offs typically associated with machine vision cameras, the results obtained from this technique correspond to detection ranges acquired by an attentive visual observer observing a limited field of view under similar environmental conditions. The technique scales with environmental conditions although dust, smog, and other inclement weather may necessitate the use of a more complex atmospheric transfer function. Note that the circumstances as described define the ideal scenario. An unaware or distracted observer is expected to perform poorly, potentially significantly more, depending on prevailing conditions.

### A. Derivation of $R_0$

From a signal perspective, $R_0$ is the maximum range where the target possesses sufficient contrast against the background and noise floor to be detected with a high probability via an automated detection algorithm. As such, $R_0$ fuses the radiometric and geometric detection properties of the target into a singular, distinct figure of merit. The theoretical $R_0$ is defined as the range at which the target of interest subtends exactly one pixel in the absence of intermediate transfer functions and point-spread effects. This is the minimum required for an automated image processing algorithm to reliably extract the target.

The Convair 580 has a nominal wingspan of 32 m, a nominal height of 8.2 m including the tail section, and a fuselage only diameter (75% of height) of 6 m. Given a camera system with a lens focal length of $f = 12\ \mathrm{mm}$ and a detector array pixel pitch of $d_{pix} = 3.45\ \mu\mathrm{m}$, the instantaneous field of view of a single pixel($w_{pix}$) is given by Eq. 1 [3],

$$\omega_{pix} = 2\arctan\left(\frac{d_{pix}}{2f}\right) = 2\arctan\left(\frac{3.45\times10^{-3}\ \mathrm{mm}}{2\times12\ \mathrm{mm}}\right) = 0.287\ \mathrm{mrad} \tag{1}$$

The resultant angular resolution corresponds to the visual acuity of the human eye under ideal physiological conditions. Under a thin-lens assumption (where the distance to the target is much greater than the focal length), the ratio between pixel-pitch and focal length is equivalent to the ratio between the subtended object dimension, $d_{obj}$, and distance/range $Z$ (Eq. 2),

$$\frac{d_{pix}}{f} = \frac{d_{obj}}{Z} \tag{2}$$

Assuming that $Z = R_0$, the maximum range for detecting an aircraft can be estimated if the target dimension is available. Inbound aircraft near the horizon detected by a ground observer presents a minimal frontal aspect dominated by the fuselage. The Convair, specifically, has a fuselage cross-section of $d_{obj} = 6\ \mathrm{m}$, which corresponds to the derived $R_0$ in Eq. 3

$$R_0 = \frac{d_{obj}}{2\cdot\tan\left(\frac{\omega_{pix}}{2}\right)} = \frac{6\ \mathrm{m}}{2\cdot\tan\left(\frac{2.87\times10^{-4}\ \mathrm{mrad}}{2}\right)} = 10.4\ \mathrm{km} \tag{3}$$

The theoretical $R_0$ is degraded by intermediate transfer functions that limit the target resolution and contrast.

### B. Intermediate Transfer Functions

For an airborne target, the net transfer function is a combination of atmospheric, motion and optical effects.

$$M_A(t) * M_V(t) * M_O \tag{4}$$

Here, $M_A(t)$ is a time-dependent atmospheric transfer function, albeit quasi-static, $M_V(t)$ is platform motion (also time-dependent) and $M_O$ is the optical transfer function for the lens and detector array. Given a calibrated camera and a fixed camera installation (ground observer), signal degradation is primarily due to the atmosphere. Under a quasi-static atmospheric model, contrast to the target is limited by atmospheric extinction and scattering effects as a function of range. If the atmosphere is modeled as a finite homogeneous medium, where optical effects are dominated by absorption and Rayleigh scattering, the target signal through a section of the atmosphere can be modeled by the Beer-Lambert law,

$$I_{out} = I_0 \exp^{-\sigma R} + B_0(1 - e^{-\sigma R}) \tag{5}$$

where $I_0$ is the source intensity of the target incident on the section, $B_0$ is the incident background radiation intensity, and $I_{out}$ is the exit irradiance from the medium as a sum of incident intensities weighted by the extinction coefficient, $\sigma$. The extinction coefficient may be approximated from the local METAR visibility profile via Koschmeider's formula,

$$\sigma \approx \frac{3.912}{V}, \quad \text{where } \lambda = 550 \text{ nm} \tag{6}$$

where $V$ denotes the visibility in units of meters. Prior experiments confirm that the atmospheric extinction model dominates other transfer functions for long-range targets under ambient illumination when viewed against a blue-sky background [4].

### C. Empirical Contrast-To-Noise Ratio

The contrast-to-noise ratio (CNR) can be measured from target pixel intensity measurements as follows,

$$CNR = \frac{\mid d_s - d_b \mid}{d_n}, \tag{7}$$

where $d_s$ is the target signal, $d_b$, the local average background signal, and $d_n$, the noise floor, all measured in pixel intensity value or digital number [dn]. The absolute value ensures that CNR is equally meaningful whether the target is lighter or darker than the background. Recall that the incident irradiance on the sensor is a function of the source radiance modulated by intermediate transfer functions. Since motion is non-existent, the optics and detector transfer functions are fixed, linear, and time-invariant, the incident radiance is equivalent to the atmospheric exit radiance $I_{out}$ as derived previously. By tying the exit radiance to CNR estimates, experimental $R_0$ estimates can be derived from experimentally extracted CNR values.

Given a sequence of image captures of an inbound aircraft, the target per image can be extracted by a Shi-Tomasi corner detector [5]. Similarly, the local background is extracted by averaging the region of interest surrounding the target, while the noise floor is estimated apriori from the sensor noise. Applying the CNR equation generates a single estimate per image. Given that each frame is also correlated to the aircraft position, and by extension, distance from the sensor, the sequence of CNR observations can be plotted as a function of range. Under the scenario where the atmospheric extinction dominates, an exponential fit function is appropriate (Eq. 8).

$$CNR(R) = a \exp^{-\sigma R} \tag{8}$$

Here, the fit parameters are the extinction coefficient, $\sigma$, and a linear scaling parameter, $a$. Under a Gaussian ergodic process assumption, a threshold of $CNR_{th} = 5$ maps to a 90% detection probability and a 1% false alarm rate [6]. Then, the experimentally derived $R_0$ can be estimated from the intersection of the fitted curve and the threshold (Eq. 9).

$$R_{0,exp} = \frac{\ln a - \ln CNR_{th}}{\sigma} \tag{9}$$

Similarly, precision of the fitted $R_0$ estimate can be computed from the calculus of errors, as per Eq. 10,

$$\delta R_0 = \sqrt{\left(\frac{\delta a}{a \cdot \sigma}\right)^2 + \left[\frac{\delta a}{\sigma^2}(\ln CNR_{th} - \ln a)\right]^2} + \delta R_{sys} \tag{10}$$

where $\delta R_{sys}$ represents the systematic error. Further details regarding the derivation are available in [7]. A key advantage of this approach is the ability to robustly extract $R_0$ from partial observations from a subset of the flown track.

## III. Experimental Setup

Flight tests were conducted on August 16th, 2017 at the Smith's Falls – Montague airfield in southeastern Ontario, located at 45.322500 N, 75.669167 W (Figure 1). The National Research Council of Canada's Flight Research Laboratory supplied a fully instrumented Convair 580 test platform for conducting low-flying tracks for audibility and visual detectability analysis. The Convair is a twin turbo-prop, light passenger aircraft with a visual and acoustic profile similar to that of typical commercial traffic, and therefore, is a good representative of such.

**Figure 1. Birds-eye view of the Smiths Falls-Montague Airport with the yellow dot indicating the camera position and the red vector indicating the viewing direction**

The sensor hardware consisted of a Genie Nano GigE M2450 camera manufactured by Teledyne Dalsa mated to a Schneider Cinegon C-mount fixed focal-length lens with a focal length of 12 mm and a maximum aperture of $f/1.4$. The camera was operated in portrait mode to maximize the vertical field of view. The M2450 contains a Sony Pregius IMX250: A monochrome global-shutter image sensor with a resolution of $2448 \times 2050$ pixels, a pixel pitch of 3.45 $\mu$m and an aspect ratio of 2/3-inches. Although capable of recording at 12 bits of dynamic range, the sensor was operated in 8-bit mode for the present flight tests for ease of recording and visual inspection. The recorded images were GPS time-stamped for offline synchronization with the aircraft data acquisition system.

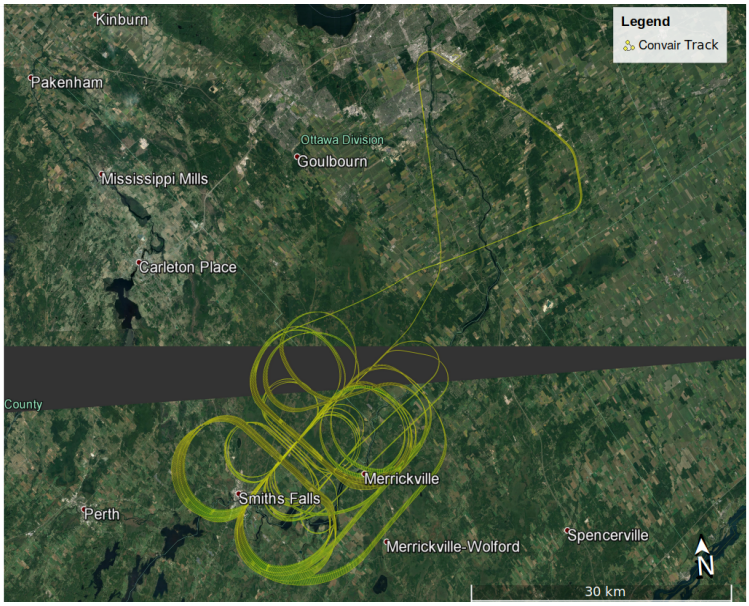


**Figure 2. Flight path of the Convair 580 overlaid onto the test site (© Google Earth)**

Test tracks were designed to simulate typical behaviour of low-flying aircraft, including ingress, egress and loi-

tering, and consisted of glide-slope inbounds at a fixed descent rate coupled with level-flight cloverleaf patterns at multiple fixed altitudes (Figure 2). Acoustic and visual measurement systems were operated concurrently from fixed locations for the duration of the test. Given the camera's position and limited field of view, visual detection analysis was restricted to runway-aligned glide-slope inbound tracks and level-flight inbound and outbound legs of the cloverleaf pattern. A representative subset of the collected events were selected for analysis.

# IV. Results and Analysis

Each event was processed by an image processing pipeline similar to the one described in earlier work [8]. The output of each event is a sequence of CNR values plotted as a function of range, where the range is derived by synchronizing the image GPS time-stamp to the aircraft position. CNR plots from the individual events are presented in Figure 3. In each plot, the raw CNR observations extracted from the captured imagery are illustrated as blue dots. The observations are fitted to a curve (depicted in red) via a constrained least-squares fit, where the fit function is a decaying exponential corresponding to Eq. 8. The per-plot legend captures the estimated parameter values and the associated uncertainty. The maximum detection range, $R_0$, and its associated uncertainty, $\delta R_0$ are computed from the fit parameters $a$ and $b$ (where $b = \sigma$), as per Eqs. 9 and 10 respectively. In the plot, the $R_0$ value is visually represented by the intersection of the red (fitted) curve and the threshold line. Results are summarized in Table 1. In cases where the CNR is too noisy at long ranges due to signal artifacts and ground clutter, the extracted $R_0$ represents an extrapolation derived from the curve fit and the error is correspondingly greater. Note that some events are repeats of a prior approach and are included for robustness.

## A. Event 1 - Glide-slope 1

The first event depicts a glide-slope inbound track along the 024 approach. Each glide-slope inbound track was commenced at a range of 20 km from the airstrip and a nominal altitude of 3000 ft. The Convair then descended at a nominal descent rate of 750 ft/min to accommodate its performance envelope and a nominal airspeed of 155 kts. The aircraft resumed level flight at 500 ft, which was calculated to coincide with the start of the runway.

Figure 3a depicts the CNR curve as a function of range for this event. The target signal exceeded the noise and clutter floor at just under 10 km. The signal drop-off at close range indicates a target departing the field of view (overhead). As such, the fit was constrained to observations between 0.5 km and 10 km. The general trend of observations is positive and correlates strongly with a decaying exponential function, as evidenced by the quality of the fit. There were few to no missed detections once the target CNR was sufficiently above the threshold ($\mathrm{CNR_{th}} = 5$). From Eqs. 9 and 10, the experimental maximum detection range can be computed as $R_0 = 7.43 \pm 0.063$ km. It is noted that ground-based visual observers were able to spot the Convair from its smoke contrails well before the actual aircraft was sighted. Visual inspection of captured imagery from Event 1 revealed prominent controls that can potentially enlarge the apparent target size. Contrails were noticeable on both glide-slope inbounds, and on all low-altitude level inbound passes over the runway.

## B. Event 2 - 1000 ft Inbound

This event represents the first level-flight inbound segment along the 024 approach at an altitude of 1000 ft (Figure 3b). The aircraft flew at a nominal airspeed of 155 knots for all inbound legs. Subsequent inbounds follow a similar pattern to this event, although true tracks are varied due to altitude differences and track drift. Figure 3b illustrates the CNR observations and fitted curve as a function of distance. The upper and lower fit bounds were chosen to be 8.0 and 2.0 km respectively to accommodate the target's presence in the camera's field of view. A detection range of $R_0 = 6.93 \pm 0.14$ km is computed from the fit values. Note that signal fluctuations are stronger than Event 1, suggestive of specular reflections. However, the technique is robust against specular reflections and impact on the computed value is limited as a result. Additional outliers are observed in the noise floor indicating systematic bias, the cause of which is unclear.

## C. Event 8 - 1000 ft Inbound (repeat)

This event depicts a repeat of Event 2, albeit the image sequence starts at a lower range of 6 km (Figure 3c). The signal is well above the noise floor for the duration of the sequence given the relative proximity of the target. Upper and lower bounds are limited to 5 km and 1 km respectively. Despite these constraints, the model is robust enough to predict the maximum detection range, albeit with a corresponding increase in the $R_0$ uncertainty. Strong target fluctuations are observed, corresponding to abnormally high CNR values attributed to ground clutter fluctuations. The

target is presumed lost between 3.5 and 4 km, confirmed by visual inspection of the image sequence (target disappears into the clouds). Given the fit parameters, a maximum detection range of $R_0 = 8.78 \pm 0.23$ km is observed. The correspondingly larger error is primarily due to target fluctuations and false positives.

### D. Event 9 - 2000 ft Inbound

This event depicts a level-flight inbound leg of the cloverleaf pattern flown at an altitude of 2000 ft. The inbound leg starts at a distance of 8 km from the camera installation. The cloud ceiling consists of broken clouds and is significantly lower than prior events (a local METAR profile was not available to confirm). High-contrast artifacts located at the edges of cloud structure yielded multiple false positives during the signal detection stage. Figure 3d illustrates the CNR plot as a function of range. Strong fluctuations can be observed at long ranges (abscissa values greater than 5 km) primarily due to a high rate of false positives, further compounded by the low CNR of the true target. Detection reliability is observed to improve with decreased range; however, the absence of a full-fledged tracker leaves the detections vulnerable to sporadic false positives, resulting in wild oscillations of the target CNR.

The fit quality is poor compared to Events 1, 2 and 8, detrimentally affecting the observed $R_0$ precision. Upper and lower bounds for the fit constraints were limited to 5 km and 1.5 km respectively. Subsequently, a maximum detection range of $R_0 = 10.1 \pm 0.27$ km can be observed from the fit parameters. Since the derived $R_0$ is extrapolated in this case, the associated fit error is correspondingly larger. The present $R_0$ is larger than earlier measurements but can be explained by the sun approaching its zenith during this event, which maximized background illumination, thereby maximizing the observed CNR.

### E. Event 11 - 2000 ft Inbound Repeat

This event is a repeat of Event 9, with the CNR observations and fit captured in Figure 3e. The sequence starts at approximately 6.8 km, which, given the results from Event 8, suggests that CNR values will remain well above the noise floor for the duration of the track. The closest point of approach is within 500 m, however, the closest observable point occurs at approximately 1.2 km. Missed detections and false positives are observed at various points throughout the sequence. Strong undulations in CNR values suggest a periodic effect, likely due to moving cloud cover and high-contrast artifacts from cloud fringes interfering with the target signal. Inspection of the individual signal and background curves indeed confirms that these periodic moments are due to background fluctuations, suggesting that a more robust background estimation technique may be desired. The CNR never settles near the noise floor suggesting a higher than average detection range. The fact that the sun was roughly at its zenith for the day may prove to be a contributing factor.

The fit function is constrained between the start of the sequence (6.8 km) and the point at which the target disappears from the field of view (1.0 km). Errors from the fit parameters are relatively low compared to other events, suggestive of a good fit. The computed detection range from the fit parameters reveals an $R_0 = 14.7 \pm 0.36$ km . It is noted that this range is significantly greater than previous events.

### F. Event 12 - Glide-slope 2

The final event under consideration is a glide-slope inbound event as a repeat of Event 1. Although more events were captured, the combination of low-flying clouds in the afternoon and extremely high altitudes meant most of the subsequent events were unsuitable for analysis. In this particular case, much like Event 1, the track commenced at a range of 20 km and a nominal altitude of 3000 ft, with the aircraft resuming level-flight at an altitude of 500 ft, timed to coincide near the start of the runway. An average airspeed of 155 knots was maintained for the duration of the track. The CNR observations and fitted curve are presented in Figure 3f. Unlike Event 1 however, the significant presence of scene clutter and lack of a tracker result in spurious detections and false positives at long ranges. The upper bound for the fit function was correspondingly limited to 6.5 km, while the lower bound was limited to 500 m, the point at which the target disappeared from the field of view.

A single strong oscillation in the observed CNR values is observable between abscissa values of 3 km and 4 km, the smooth shape of which cannot be attributed to false positives alone. It is hypothesized that a course correction at the 4 km mark resulted in an apparent aspect change, which, coupled with the time of day (roughly noon), dramatically altered the observed CNR. Given the fit parameters and errors, the detection range is computed to $R_0 = 8.67 \pm 0.17$ km, which is surprisingly similar to Event 1, although beyond the margin of error overlap. It is noted that the CNR value is 140 at the closest point, indicating a strong difference between target and background intensity values. Inspection of the signal and background intensity values confirms a target intensity value of 50 dn and a background intensity value of 225 dn as the cause of the difference. Therefore, not only is the target much darker than the background at

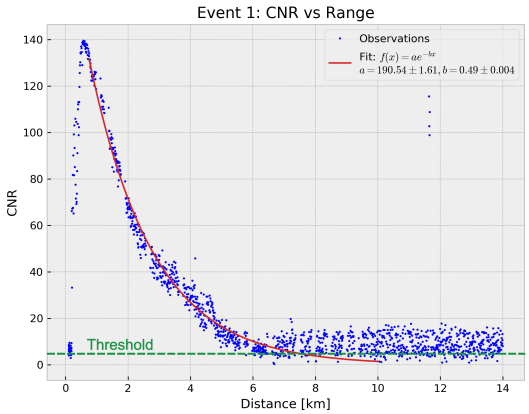


**a) Event 1**

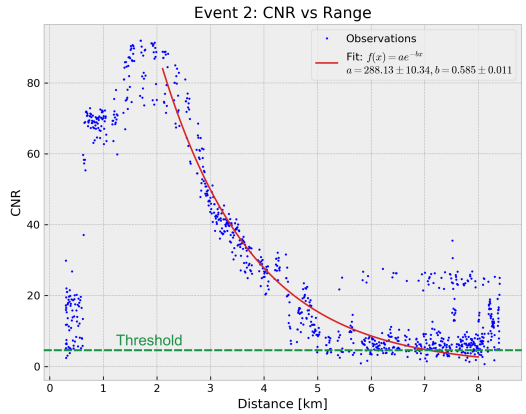


**b) Event 2**

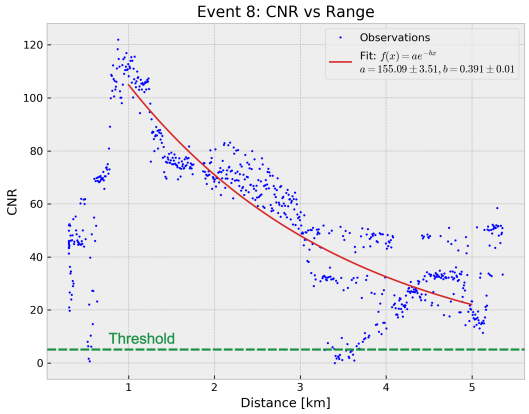


**c) Event 8**

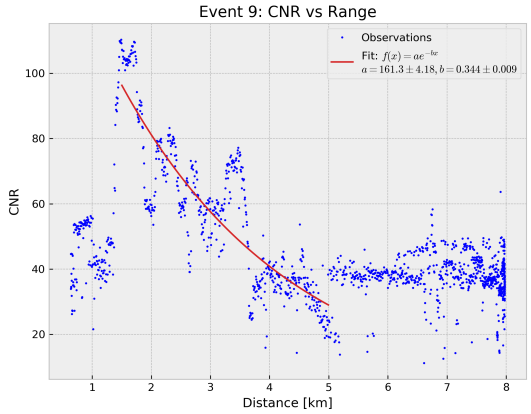


**d) Event 9**

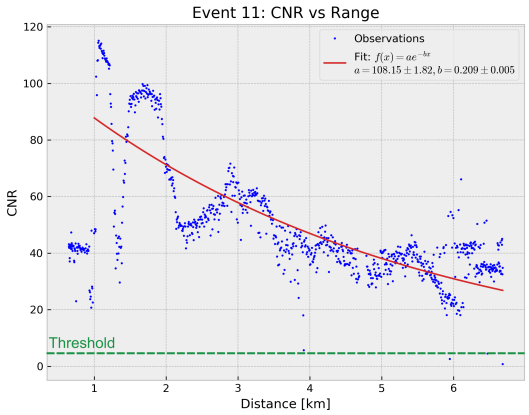


**e) Event 11**

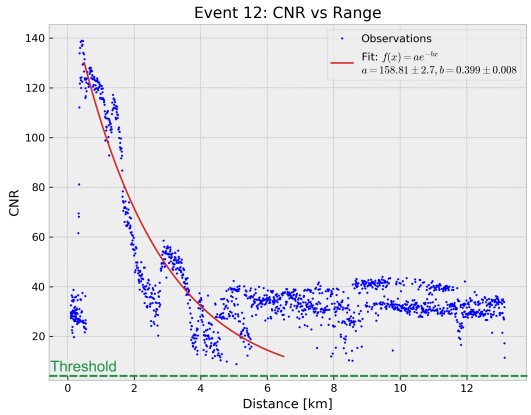


**f) Event 12**

**Figure 3. Contrast to Noise Ratio (CNR) plot as a function of range for glide-slope and level inbound events. Blue dots denote individual CNR values (one per image), while the red curve denotes the exponential fit. Fit parameters are presented in the legend along with error estimates. The threshold for calculating $R_0$ is denoted as a green dotted line and fixed at $CNR = 5$ for all events. Note that the threshold is below the y-axis limits in Event 9.**

the closest observable point of approach, but the separation between target and background is approaching the limit of the camera's dynamic range. Note that exposure and aperture settings were constant for the duration of the test. This is not an unexpected occurrence however, given that the time of day was roughly noon for this event.

### G. Summary of Findings

Table 1 captures the results of the analysis from individual events. The average maximum detection range, $\overline{R_0}$ represents the best estimate of the maximum detection range from individual events. $\overline{R_0}$ is computed by taking the weighted average of the individual $R_0$ values as per Eq. 11,

$$\overline{R_0} = \frac{\sum_{i=1}^{N} w(i) \cdot R_{0,i}}{\sum_{i=1}^{N} \omega_i}, \quad \text{where } \omega_i = \frac{1}{\sigma_i^2} \tag{11}$$

Here, $N$ is the total number of events, while each $R_{(0,i)}$ and $\sigma_i$ are the measured detection range and corresponding standard deviation for that event. Similarly, the uncertainty in the weighted average can be computed as per Eq. 12,

$$\overline{\sigma_{R_0}} = \frac{1}{\sqrt{\sum_i^N = 1\omega_i}} \tag{12}$$

A weighted mean was computed from the events for an average estimate of $R_0 = 7.78 \pm 0.05$ km, suggesting that the Convair 580 has a high probability of detection at $\sim 8.0$ km under high-visibility conditions. The estimated $R_0$ will degrade accordingly for a distracted observer and inclement weather. A visual attention model may be needed to assess the former, while the acoustic measurements should play a strong role in establishing some of those thresholds for the latter.

**Table 1. Representative dataset for detection range analysis**

| Event | Test Point | GPS Week Time [s] | Measured $R_0$ and Uncertainty [km $\pm$ $2\sigma$ ] |
|---|---|---|---|
| 1 | Glide-slope 1 | 311411.47 | $7,43 \pm 0.06$ |
| 2 | 1000 ft Inbound | 311826.88 | $6.93 \pm 0.14$ |
| 8 | 1000 ft Inbound (repeat) | 313579.80 | $8.78 \pm 0.23$ |
| 9 | 2000 ft Inbound | 313845.52 | $10.1 \pm 0.27$ |
| 11 | 2000 ft Inbound (repeat) | 314689.54 | $14.7 \pm 0.36$ |
| 12 | Glide-slope 2 | 315061.16 | $8.67 \pm 0.17$ |
| - | - | **Weighted Average** ($\overline{R_0 \pm 2\sigma}$) | $7.78 \pm 0.05$ |

## V. Conclusions

In this paper, the visual detectability of the Convair 580 was assessed. The technique for quantitatively assessing maximum detection range was repurposed from a detect-and-avoid system for unmanned aircraft. Experiments were conducted at an uncontrolled airfield, where the Convair 580 flew a sortie of tracks simulating ingress, egress and loitering operations. A calibrated machine-vision camera with known parameters recorded the aircraft for a subset of each flown track. Results indicate that the Convair was detected at $R_0 = 7.78 \pm 0.05$ km with high probability under clear sky conditions with broken cloud cover not exceeding 20%. The estimated detection range can be suitably generalized to a typical Convair-sized aircraft assuming high visibility conditions and an attentive visual observer equipped with unimpaired vision. Significant variability was observed in the $R_0$ values computed from individual events and primarily attributed to variations in the environment and the background estimation technique. Future work will focus on evaluation with other aircraft and software improvements in the background estimation portion of the technique, either via use of Gaussian mixture models or other statistical estimation process.

## Acknowledgments

The authors thank the efforts of pilots Anthony Brown and Paul Kissmann for operating the Convair, Robert Erdos for ground-crew radio coordination, and Jiaxin Liu for software development effort and operation of the camera system.

# References


[1] Brady, D., Gehm, M., Stack, R., Marks, D., Kittle, D., Golish, D., Vera, E., and Feller, S., "Multiscale gigapixel photography," *Nature*, Vol. 486, No. 7403, 2012, pp. 386–389.

[2] Andrews, J., "Unalerted Air-to-Air Visual Acquisition," Tech. Rep. ATC 152, Lincoln Laboratories, MIT, Lexington, MA, November 1991.

[3] Born, M. and Wolf, E., *Principles of Optics: Electromagnetic Theory of Propagation, Interference and Diffraction of Light*, Cambridge University Press, 7th ed., 1999.

[4] Minwalla, C., Ellis, K., and White, J., " Experimental Evaluation of PICAS: An Electro-Optical Array for Non-Cooperative Collision Sensing on Unmanned Aircraft Systems," *Proc. AIAA Information Systems-AIAA Infotech @ Aerospace, AIAA SciTech Forum*, Jan 2017, pp. 1–20.

[5] Shi, J. and Tomasi, C., "Good Features to Track," *Proc. IEEE Conference on Computer Vision and Pattern Recognition*, 1994, pp. 593–600.

[6] Holst, G. C., *Electro-optical Imaging System Performance*, SPIE Press, 3rd ed., 2003.

[7] Minwalla, C., Thomas, P., Hornsey, R., Ellis, K., and Jennings, S., "Range performance evaluation from the flight tests of a passive electro-optical aircraft detection sensor for unmanned aircraft systems," *Journal of Unmanned Vehicle Systems*, Vol. 4, No. 2, Feb. 2016, pp. 96–114.

[8] Minwalla, C., Tulpan, D., Belacel, N., Famili, F., and Ellis, K., "Detection of airborne collision-course targets for sense and avoid on unmanned aircraft systems using machine vision techniques," *Unmanned Systems Journal*, Vol. 4, No. 4, Nov 2016, pp. 1–18.